# Supporting Information

## Strain-controlled decomposition efficiency of $LaCoO_3$ perovskite epitaxial thin films

*Jie Tu[a,‡], Siyuan Du[a,‡], Hangren Li[a,b,‡], Jing Xia[c,]*, Longyuan Shi[a], Jianjun Tian[a], Linxing Zhang[a,d,]**

[a] Institute for Advanced Materials Technology, University of Science and Technology Beijing, Beijing 100083, China.

[b] State Key Laboratory of New Ceramics and Fine Processing, School of Materials Science and Engineering, Tsinghua University, Beijing 100084, China.

[c] Key Laboratory of Photochemical Conversion and Optoelectronic Materials, Technical Institute of Physics and Chemistry Chinese Academy of Sciences, Beijing, 100190, China.

[d] Institute of Solid State Chemistry, University of Science and Technology Beijing, Beijing 100083, China.

* Corresponding author: Prof. Jing Xia; Prof. Linxing Zhang
Jing Xia, E-mail address: xiajing@mail.ipc.ac.cn
Linxing Zhang, E-mail address: linxingzhang@ustb.edu.cn

‡ These authors contributed equally to this work.

# METHODS

## Preparation of sacrificial and target films

1.1 $LaCoO_3$

The required amount with a molar ratio of 1:1 of Lanthanum nitrate hexahydrate ($La(NO_3)_3 \cdot 6H_2O$, Aladdin, 99.99%) and Cobalt(II) acetate tetrahydrate ($C_4H_6CoO_4 \cdot 4H_2O$, Macklin, 99.5%) were dissolved in 2-Methoxyethanol ($C_3H_8O_2$, Aladdin, 99.5%). Then, the mixed solution was heated and stirred on a hot plate at 75 ℃ for 2 hours to obtain a red transparent precursor solution. Finally, the solution was filtered at room temperature.

The precursor solution was spin-coated onto 10×10 $mm^2$ STO or LAO substrates at 5000 rpm for 30 seconds. Then, it was heated on a hot plate at 120 °C for 3 minutes to remove moisture and at 350 °C for 10 minutes to eliminate the organic solvent. Finally, the LCO film was annealed in a muffle furnace at 650 °C for 30 minutes. The dimensions of STO or LAO substrates can be replaced to dimensions of 5×5 $mm^2$ or 5×3 $mm^2$. We control the film thickness of the LCO sacrificial layer by adjusting the number of spin-coating cycles. Through STEM analysis, it can be seen that the thickness of each layer is ~ 20 nm.

1.2 $PbZrO_3$

The required amount with a molar ratio of 1:1 of Lead nitrate ($Pb(NO_2)_3$, Aladdin, 99.999%) and Zirconium nitrate ($Zr(NO_3)_4 \cdot 5H_2O$, Boer, 99.99%) were dissolved in 2-Methoxyethanol ($C_3H_8O_2$, Aladdin, 99.5%). Then, the mixed solution was heated and stirred on a hot plate at 75 ℃ for 2 hours to obtain a colorless transparent precursor solution. Finally, the solution was filtered at room temperature.

The precursor solution was spin-coated onto 10×10 $mm^2$ LCO/STO or LCO/LAO substrates at 5000 rpm for 30 seconds. Then, it was heated on a hot plate at 120 °C for 3 minutes to remove moisture and at 350 °C for 10 minutes to eliminate the organic solvent. Finally, the PZO film was annealed in a muffle furnace at 750 °C for 30 minutes.

1.3 Directional electrodynamic decomposition

Using a 304 stainless steel clip, it can grasp a corner of the PZO films. This clip is affixed to the anode of the current source. Subsequently, the cathode of the current source is then connected to the carbon rod, which should then be immersed in an 10% $CH_3COOH$ solution. The applied current is 2 A with the voltage of 10 V for PZO films.

During the preparation process, the applied voltage and the selection of the solution for decomposition are crucial. Although high applied voltage implies an

ultrafast decomposition rate. But in fact, for the PZO films, there is a voltage threshold of ~ 25 V. When the applied voltage exceeds 25 V, it may cause the break of the PZO target layer. It is worth noting that when we separate the $BiFeO_3$ films and $BiSmFe_2O_6$ double perovskite films, this value is only ~ 1 V [1]. We consider that this is related to the resistivity of the target layer. In fact, the LCO sacrificial layer can decompose not only in acetic acid solution but also in salt solution. For target layer materials with similar resistivity, choosing different solutions can enable the self-support of this type of target layer. We employ the ultra-fast directional electrodynamic decomposition technology to achieve the rapid decomposition of the LCO sacrificial layer, which ensures the flatness and non-damage of the target layer.

**Characterization methods**

2.1 X-ray diffraction

The structure and orientation of the LCO thin films were investigated using X-ray diffraction (XRD) with Cu *K*α radiation (XRD, 1.54178 Å, PANalytical X'Pert Powder PW3040/60, Holland). The out-of-plane lattice constant of the film can be calculated using the Bragg equation: $n\lambda = 2d\sin\theta$, where $\lambda$ is the wavelength of the X-rays, $d$ is the interplanar spacing, and $\theta$ is the diffraction angle. Synchrotron-based RSM and rocking curves (1W1A beamline of the Beijing Synchrotron Radiation Facility, China) were used to prove the strain relaxation and epitaxial growth of LCO thin films on different substrates, respectively.

2.2 Transmission election microscope

The atomic-resolution STEM images, revealing atomic arrangements and film thickness, were acquired using spherical aberration-corrected HAADF scanning transmission electron microscopy (ARM300F/GRAND-ARM, JEOL, Japan) operated at an acceleration voltage of 300 kV. The EDS mapping based on HAADF- STEM was used to observe the positions of the atoms. Given the known lattice constants of STO (3.90 Å) and LAO (3.79 Å) substrates, we correct the lattice constants of LCO films.

2.3 UV-Vis absorption spectra

The UV-visible absorption spectra of LCO thin films were measured using a UV-visible spectrophotometer (UV-Vis, T10CS, PERSEE, China). We measured the absorption value of the film/substrate structure. The uncoated substrate was used as the control sample. Therefore, the equipment would directly subtract the absorption value of the substrate, resulting in the curve graph of film. This operation was carried out by the equipment. The transmittance and absorbance are automatically converted by the

instrument. In our previous study [2], it was found that the second annealing process would cause the oxygen vacancies in the substrate to rearrange, which may imply a change in the absorption value. And we found that the substrate subjected to the second annealing process exhibited a pale orange color instead of the transparent color of the initial substrate, which may imply changes in the band gap and the light absorption [3]. During the process of reducing the low absorption value of the substrate, we employed a new double-polished substrate. This may result in the substrate's absorption value not being completely deducted. In fact, this is also the reason why the absorption values that are not zero each time have the value differences. However, the significant decrease in absorption value exhibit by the film/substrate structure and the obvious color changes show in the optical photographs cannot be ignored.

2.4 X-ray absorption spectroscopy

The X-ray absorption spectroscopy (XAS, 4B9B beamline of Beijing Synchrotron Radiation Facility, China) was used to study the Co-O octahedral distortion in LCO thin films.

2.5 X-ray photoelectron spectroscopy

The X-ray photoelectron spectroscopy (XPS, Thermo Scientific K-Alpha, USA) was employed to analyze the chemical composition of the LCO thin films. The sample surface was bombarded with $Ar^+$ beam to study the proportion of deep elements and to evaluate the strength of Co-O bonds in the films on different substrates. The reductive nature of $Ar^+$ bombardment is a surface chemical change triggered by energy transfer. When high-energy $Ar^+$ (> 3 keV) strikes the surface of the sample, it transfers its kinetic energy to the atoms within the metal oxide, which is sufficient to break the stable Metal-Oxygen bonds. And under the XPS test conditions of vacuum environment, the reduced low-valent metals cannot re-oxidize and remain in the reduced state continuously.

2.6 Piezoresponse force microscopy

The piezoresponse force microscopy (PFM, Asylum Research, MFP-3D-Infinity, USA, Olympus AC240TM Pt/Ti-coated silicon cantilevers, China) was used to investigate the local piezoelectric response of the freestanding PZO thin films.

## Supporting figures

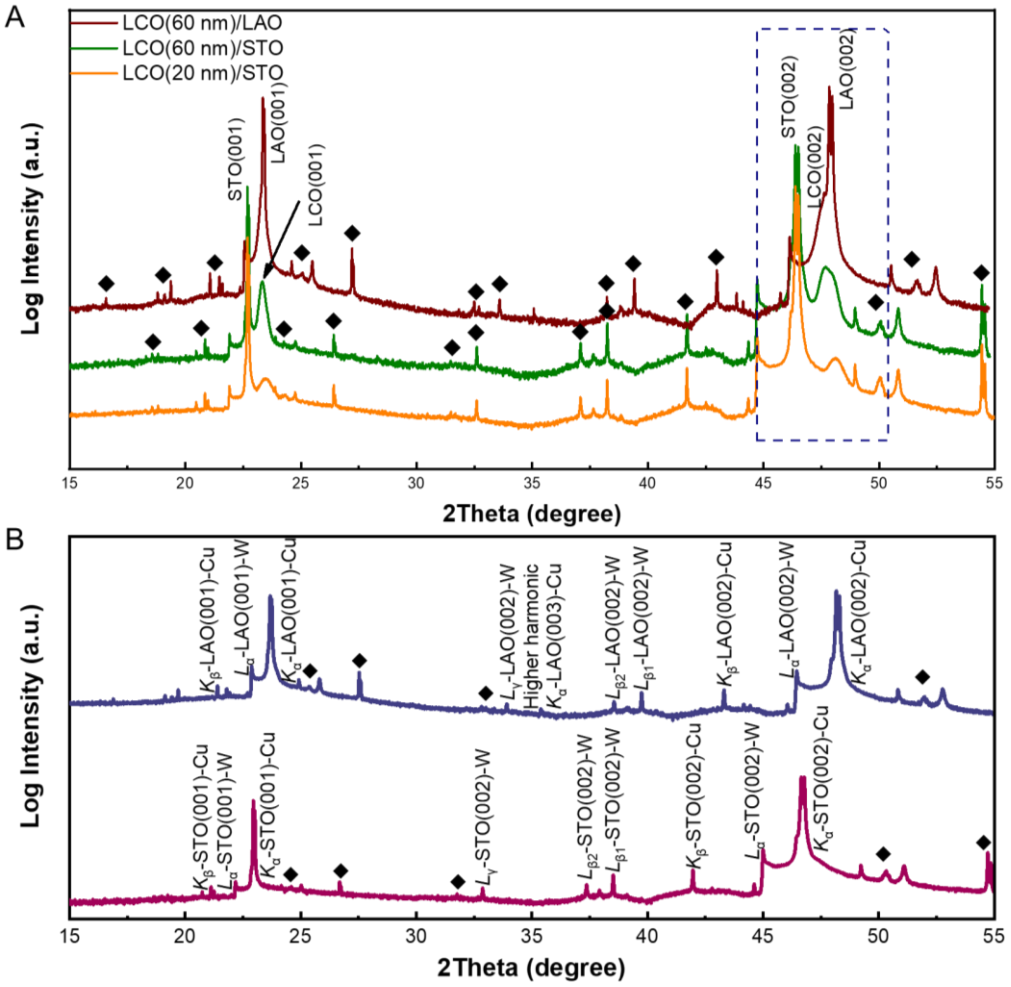


**Fig. S1** (A) XRD patterns with a large angle region of LCO (60 nm)/LAO, LCO (60 nm)/STO, and LCO (20 nm)/STO films. It is important to note that we use "◆" to label diffraction peaks originating from the LAO or STO substrates. (B) XRD patterns with the same large angle region of pure LAO and STO substrates without film coverage. The other diffraction peaks come from the diffraction of the substrate with respect to X-rays of other wavelengths, such as the diffraction peak of LAO substrates (003) plane at ~ 35.38° from the Cu $K_\alpha$ X-ray diffraction with second harmonics (~ 0.77 Å), the diffraction peak of LAO substrates (002) plane at ~ 33.91° from W $L_\gamma$ X-rays (~ 1.10 Å), and the diffraction peak of LAO substrates (002) plane at ~ 32.87° from W $L_\gamma$ X-rays (~ 1.10 Å). The peak of ~ 35.38° was sometimes absent in the STO substrates, which might be due to the fact that vector superposition of X-rays is difficult to occur in a common XRD diffractometer.

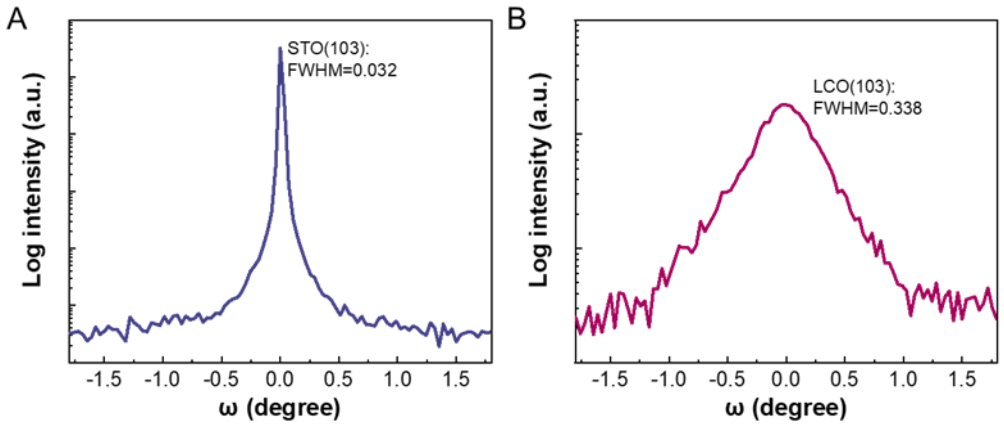


**Fig. S2 Rocking curves of LCO thin films with 20 nm on STO substrates.** (A, B) Rocking curves of STO substrates (A) and LCO thin films (B). The full width at half maxima (FWHM) of LCO films is only about 10 times that of the substrates. As is well known, the STO substrates are grown as single crystals. This means that the (103) plane of LCO films is perfectly parallel to the (103) plane of the substrates, indicating the single-crystalline nature of epitaxial LCO films.

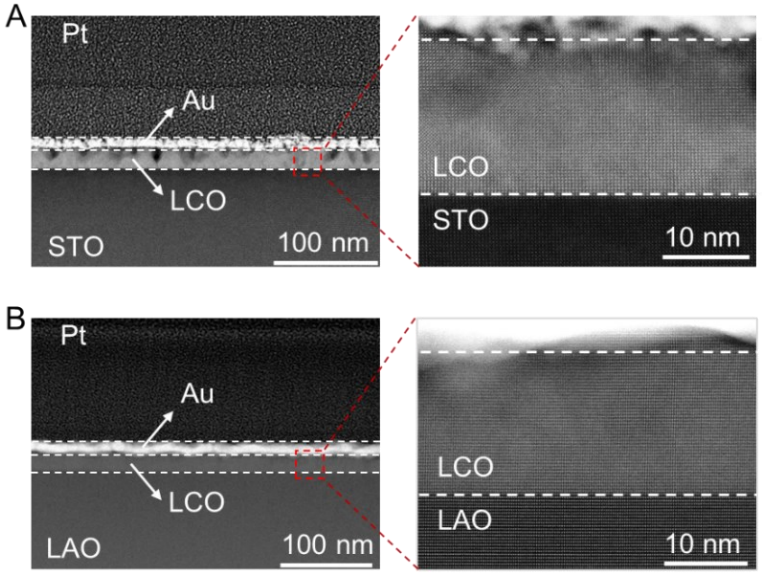


**Fig S3.** Low-magnification HAADF-STEM images and high-magnification HAADF-STEM images of the interface for LCO films on STO (A) and LAO (B) substrates. They show that the films have the high flatness. During FIB-STEM sample preparation, a Pt surface layer is applied to protect the sample.

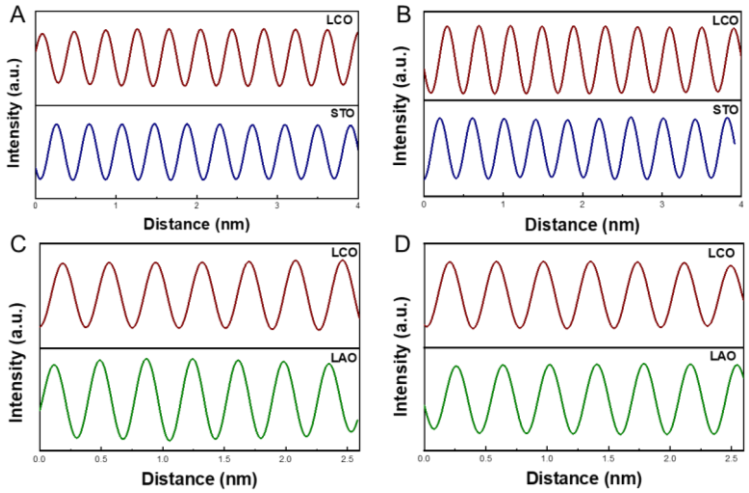


**Fig S4. Transformed small-scale HAADF-STEM images of LCO films on two substrates.** (A, C) Out-of-plane lattice spacing with *c*; (B, D) In-plane lattice spacing with *a*.

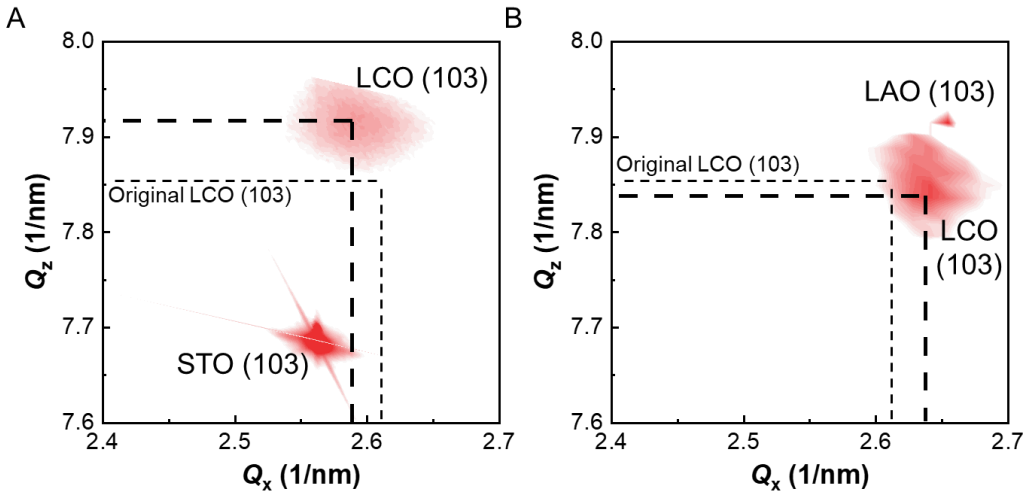


**Fig. S5. RSM patterns of LCO films with 60 nm on different substrates.** (A) RSM pattern of LCO films around STO (103) plane. (B) RSM pattern of LCO films around LAO (103) plane. We have marked the original position of the LCO with a thin dotted line, which is calculated based on its lattice constant with 3.82 Å. The diffraction peaks of LCO films on different substrates are marked with a thick dashed line.

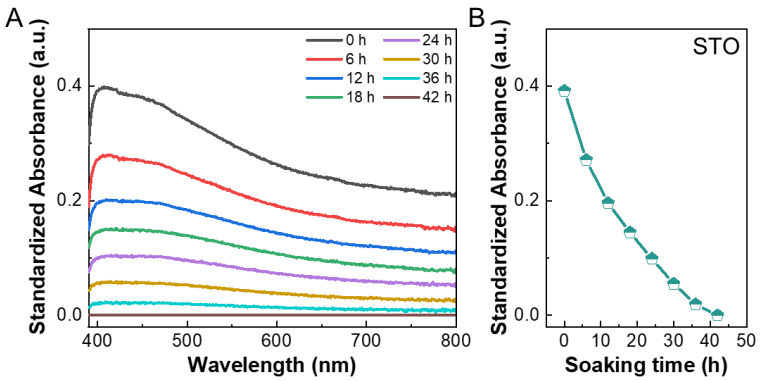


**Fig S6. Standardized optical absorption spectra of LCO thin films with 60 nm soaked in 10% $CH_3COOH$ solution.** (A) Standardized optical absorption spectra of LCO films on and STO substrates at different times. (B) Curves of standardized absorbance ($\lambda$ = 400 nm) variation of LCO films on the STO substrates with soaking time. We used the optical absorption spectrum of the LCO film on STO substrate that had been soaked for 42 hours as the reference. At this point, the LCO film had completely decomposed. This optical absorption spectrum is considered to be able to serve as the optical absorption spectrum of the corresponding annealed substrate. After eliminating the optical absorption of the STO substrate in the operation, we found that the decomposition rate of the LCO film on the STO substrate was exactly the same as that before the subtraction.

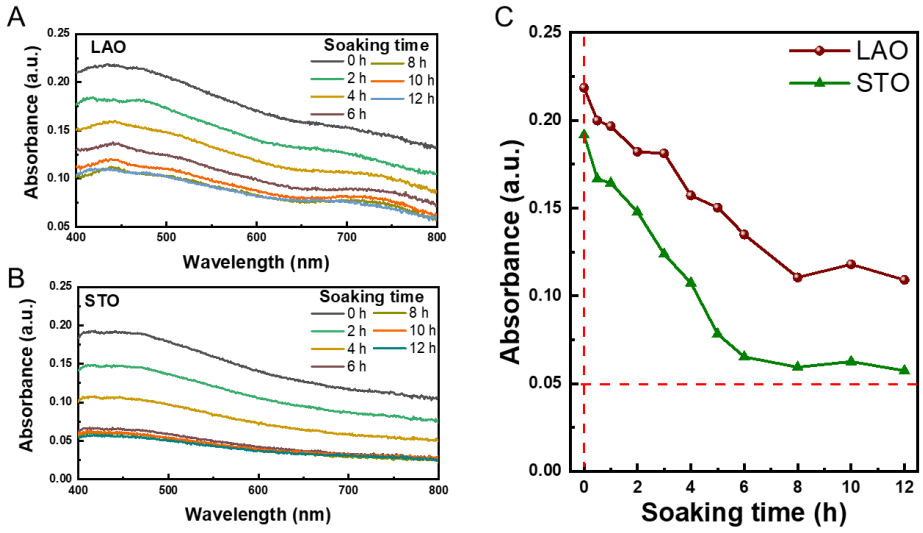


**Fig S7. LCO films with 20 nm soaked in 10% $CH_3COOH$ solution.** (A, B) Optical absorption spectra of LCO films on (A) LAO and (B) STO substrates at different times. (C) Curves of absorbance ($\lambda$ = 400 nm) variation of LCO films on two substrates with soaking time.

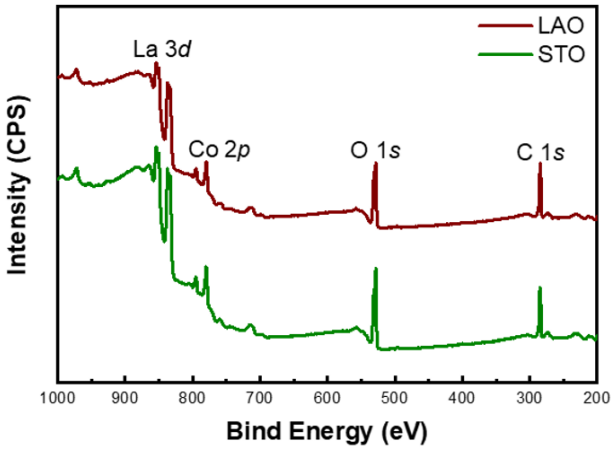


**Fig S8.** XPS full spectra of LCO thin films on the different substrates.

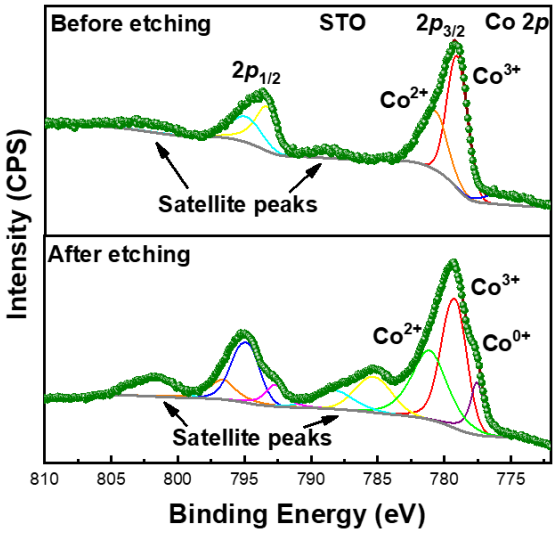


**Fig S9.** Co 2*p* XPS spectra of LCO thin films on STO substrate before and after $Ar^+$ ion etching.

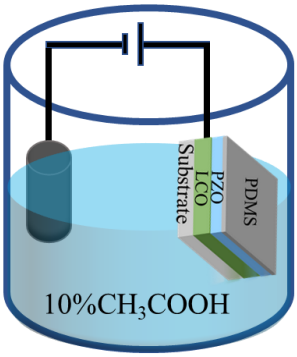


**Fig S10.** Schematic illustration of the Electrolysis process of the LCO sacrificial layer.

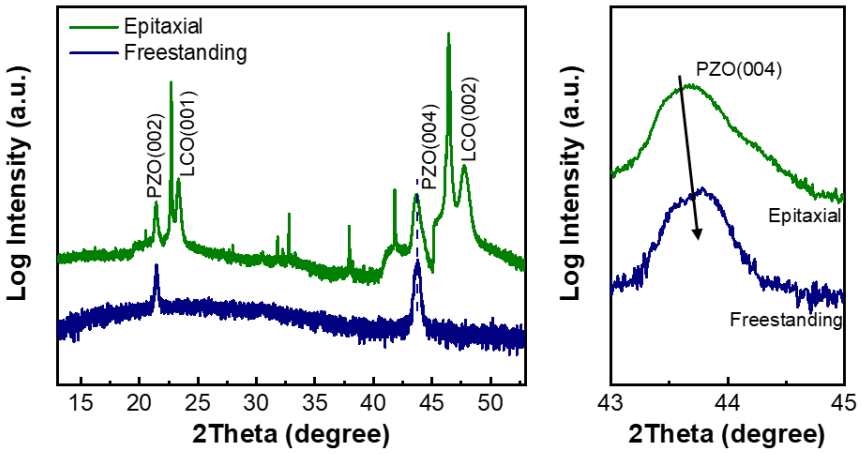


**Fig S11.** XRD patterns of PZO epitaxial thin films before and after stripping.

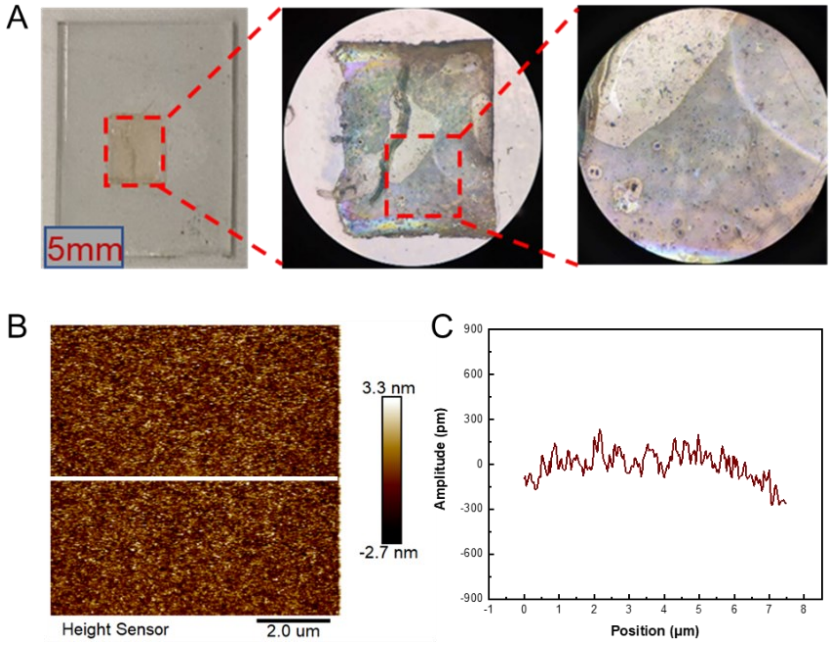


**Fig S12.** (A) Macroscopic and microscopic image of freestanding PZO film. (B) Local surface morphology of freestanding PZO film after voltage application. (C) Amplitude curve corresponding to the line segment in (B).

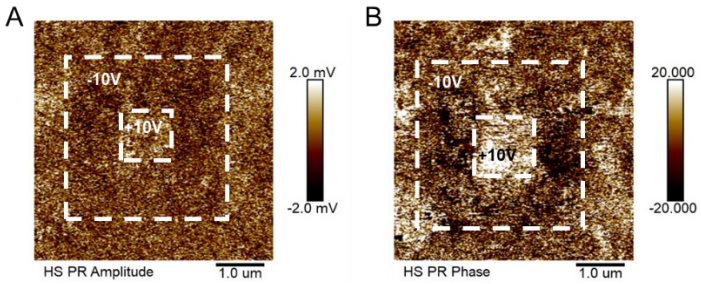


**Fig S13.** (A) Amplitude images and (B) phase inversion image of freestanding PZO film under applied voltage.

**Supporting references**

[1] J. Tu, Y.-W. Fang, Y. Lu, H. Li, G. Xi, J. Ding, X. Liu, X. Liu, Q. Yang, J. Tian and L. Zhang, Strain-controlled oxygen vacancy for robust ferroelectric $BiSmFe_2O_{6-\delta}$ double-perovskite epitaxial thin films, *Appl. Phys. Rev.*, 2024, **11**(1), 011413.

[2] H. Li, J. Tu, S. Du, G. Xi, C. Liu, Y.-W. Fang, S. Xu, J.-H. Zhang, E. Sun, S. Ouyang, X. Liu, L. Shi, X. Liu, D. Zheng, L. Guo, X. Zhang, K. Jin, J. Tian, L. Zhang and X. Xing, Efficient electrodynamic stripping for 12-inch wafer-scale freestanding ferroelectric membranes, *PREPRINT Research Square*, 2025, DOI: 10.21203/rs.3.rs-6397992/v1.

[3] P. Machado, M. Scigaj, J. Gazquez, E. Rueda, A. Sánchez-Díaz, I. Fina, M. Gibert-Roca, T. Puig, X. Obradors, M. Campoy-Quiles and M. Coll, Band gap tuning of solution-processed ferroelectric perovskite $BiFe_{1-x}Co_xO_3$ thin films, *Chem. Mater.,* 2019, **31**(3), 947-954.